RESEARCH ARTICLE | DECEMBER 09 2022

Electrolyte-gate-driven carrier density modulation and metal–insulator transition in semiconducting epitaxial CdO films

Helin Wang; William M. Postiglione; Vipul Chaturvedi; ... et. al

APL Mater 10, 121106 (2022)
https://doi.org/10.1063/5.0116294

Electrolyte-gate-driven carrier density modulation and metal–insulator transition in semiconducting epitaxial CdO films

Cite as: APL Mater. 10, 121106 (2022); doi: 10.1063/5.0116294
Submitted: 28 July 2022 • Accepted: 21 November 2022 •
Published Online: 9 December 2022

Helin Wang,[1] William M. Postiglione,[1] Vipul Chaturvedi,[1] Evan L. Runnerstrom,[2] Angela Cleri,[3] Josh Nordlander,[3] Jon-Paul Maria,[3] and Chris Leighton[1,a)]

AFFILIATIONS

[1] Department of Chemical Engineering and Materials Science, University of Minnesota, Minneapolis, Minnesota 55455, USA
[2] DEVCOM US Army Research Laboratory, Army Research Office, Research Triangle Park, Durham, North Carolina 27709, USA
[3] Department of Materials Science and Engineering, Pennsylvania State University, University Park, State College, Pennsylvania 16802, USA

[a)] **Author to whom correspondence should be addressed:** leighton@umn.edu

ABSTRACT

CdO has drawn much recent interest as a high-room-temperature-mobility oxide semiconductor with exciting potential for mid-infrared photonics and plasmonics. Wide-range modulation of carrier density in CdO is of interest both for fundamental reasons (to explore transport mechanisms in single samples) and for applications (in tunable photonic devices). Here, we thus apply ion-gel-based electrolyte gating to ultrathin epitaxial CdO(001) films, using transport, x-ray diffraction, and atomic force microscopy to deduce a reversible electrostatic gate response from −4 to +2 V, followed by rapid film degradation at higher gate voltage. Further advancing the mechanistic understanding of electrolyte gating, these observations are explained in terms of low oxygen vacancy diffusivity and high acid etchability in CdO. Most importantly, the 6-V-wide reversible electrostatic gating window is shown to enable ten-fold modulation of the Hall electron density, a striking voltage-induced metal–insulator transition, and 15-fold variation of the electron mobility. Such modulations, which are limited only by unintentional doping levels in ultrathin films, are of exceptional interest for voltage-tunable devices.

INTRODUCTION

Binary and complex oxides constitute some of the most exciting emerging semiconductors and are under intense investigation for ultra-wide-band-gap semiconductors, power electronic devices, transparent conductors and devices, high room-temperature carrier mobilities, photonic applications, and so on.[1–6] Rock-salt-structure CdO is one such binary oxide semiconductor, which has been understood to be an *n*-type transparent conductor for many years,[7–10] but is now under intense study for mid-infrared photonics and plasmonics.[11–19] Intrinsic CdO is thought to possess a relatively small (indirect) bandgap,[20,21] but can be heavily doped, inducing a large Moss–Burstein shift, and thus optical gaps >3 eV.[18,21–26] Electron doping has been achieved via oxygen vacancies (V_O)[11,21] and H[21,24,25] (which are thought to be responsible for the commonly observed high carrier densities in nominally-undoped samples[8,11]), as well as In^{3+}, Ga^{3+}, Dy^{3+}, Y^{3+}, F^-, etc.[11–13,17–19,22,26,27] Doping with such dopants is possible up to free electron densities of 10^{20}–10^{21} cm^{-3}, generating peak room-temperature mobilities >500 cm^2 V^{-1} s^{-1} and conductivity >20 000 S cm^{-1}.[11–13,18,22,26,27] Combined with low effective mass and low optical loss, these parameters enable CdO to achieve exciting photonic and plasmonic function in the difficult-to-access mid-infrared.[11–18] Specific device functions demonstrated include surface plasmon resonances,[11,13,15,17] epsilon-near-zero modes,[11,13,15,17] ultrafast optical polarization switching,[14] high harmonic generation,[16] etc., with numerous potential applications.[11–18] Importantly, well-controlled growth of CdO films enables these functions at frequencies that are at least passively tunable via chemical doping.[11–14,17,18,25]

For both fundamental and applied reasons, it would be highly desirable to *actively* control and fine-tune the free electron density in CdO films, *e.g.*, through voltage-based modulation. Fundamentally, this could elucidate the essential transport mechanisms in CdO films, including probing the mobility-electron density relation[11–13,17,18,26] in single samples, better understanding mobility-limiting scattering mechanisms,[11–13,17,18,26] and potentially probing a metal–insulator transition (CdO films are typically so heavily doped that they exhibit metallic transport). From the applied perspective, wide-range electrical control over carrier density would add an exciting additional dimension to the device potential of CdO, possibly enabling highly desirable *voltage-tuned* photonic and plasmonic devices.[28–30] Particularly given the heavy doping involved, however, such voltage-based tuning is challenging with conventional approaches such as standard field-effect transistors.[28–30]

Electrolyte gating is potentially ideal for wide-range voltage-based tuning of carrier density in CdO and has been applied to a host of other oxides,[31–33] including oxide semiconductors. The latter include ZnO,[31,34,35] In_2O_3,[36] In–Sn–O,[37] $BaSnO_3$,[38,39] $SrSnO_3$,[40] β-Ga_2O_3,[41] etc., typically in thin-film form, deposited and processed by various methods. The central device in such electrolyte gating is the electric double layer transistor (EDLT[31,32]), in which the oxide is interfaced with a high-ionic-mobility electrolyte, often an ionic liquid or ion gel. (The latter are essentially ionic liquids embedded in polymer matrices, providing high room-temperature ionic mobility in a processable solid-state platform.[32,42,43]) The essential concept is that when a gate voltage (V_g) is applied across the electrolyte, cations or anions in the liquid/gel (depending on the V_g polarity) are driven to the interface with the oxide, which they cannot penetrate. A layer of cations or anions thus accumulates in the electrolyte at the interface with the oxide, generating a large electric field. This field is then screened via the induction of a high density of electrons or holes on the oxide side of the interface (to a depth controlled by the electrostatic screening length[31–33,38,44]), forming a layer of ions and induced carriers known as an electric double layer (EDL). The power of the EDLT lies in the nanoscopic thickness of this EDL, which leads to giant specific capacitances (10s of μF cm^{-2}), decoupled from the electrolyte thickness.[31,32] At just a few volts, these capacitances induce electron/hole densities *up to* 10^{15} *cm*$^{-2}$, orders of magnitude above standard field-effect transistors.[31,32] Applied to oxide semiconductors, this has enabled exceptionally broad modulation of free electron densities, elucidation of mobility-limiting scattering mechanisms by widely varying the electron density in single films, strong mobility enhancements due to screening of charged defects, and voltage-driven insulator–metal transitions.[31,32,34–41] This is achieved at low power, due to the very small gate current densities in EDLTs, generating much device potential.[31,32]

It must be emphasized, however, that the true operating mechanisms of electrolyte-gate transistors are not necessarily based solely on simple electrostatics. In some oxides, for example, the large electric field generated by the EDL also actuates electrochemistry, particularly, though not exclusively,[31,32,45,46] via oxygen vacancy (V_O) formation/annihilation.[31,32,45,47–51] Positive V_g, for example, can remove oxide ions from oxides, doping them electrochemically via V_O.[31,32,45,47–51] Remarkably, these V_O can often be refilled at negative V_g, leading to reversible, non-volatile, electrochemical gate effects, electrolysis of residual H_2O providing the oxygen for reoxidation.[32,33,45] Other oxides, however, exhibit an electrolyte gate response that is predominantly, or even exclusively, due to simple EDL charging.[31–33] The relative contributions from these electrochemical and electrostatic gating mechanisms have been deconvoluted via transport measurements of volatility and reversibility,[45,47,52] measurement in O_2-rich atmospheres,[47,52] and by applying various *operando* probes, particularly scattering-[45,49,51,53] and spectroscopy-based.[54,55] Great strides have thus been made in mechanistic understanding, culminating in the recent publication of the first hypothesis regarding the key factors that dictate electrostatic vs electrochemical response to electrolyte gating in a given material.[33] Within this framework, the ambient-temperature diffusivity of the lowest-energy defects, often V_O in oxides, controls this process.[33] When these diffusion coefficients are negligible, for example, regardless of the defect formation energy, simple electrostatic gating mechanisms tend to prevail, due to the inability to proliferate V_O over non-negligible distances into oxide films.[33]

In light of the above, here, we apply ion-gel-based electrolyte gating to epitaxial CdO(001) films for the first time, seeking to deduce the active gating mechanisms, rationalize those mechanisms, and thus achieve highly-desired wide-range active modulation of free electron density and transport. Initial studies on relatively-thick (15–17 nm) films first combine transport measurements with pre- and post-gating characterization via high-resolution x-ray diffraction (HRXRD) and atomic force microscopy (AFM) to establish mechanisms (i.e., electrostatic vs electrochemical). Reversible electrostatic gating is deduced over a wide window (-4 V $< V_g <$ +2 V), followed by the rapid onset of film degradation above +2 V, confirmed by HRXRD and AFM. These results are interpreted in terms of low-ambient-temperature V_O diffusivity in the CdO rock-salt structure, resulting in electrostatic response to electrolyte gating, limited only by the low acid-etch stability of CdO, which leads to surface degradation above +2 V. CdO thus provides another interesting test-case that advances the mechanistic understanding of electrolyte gating. Most importantly, the -4 V $< V_g <$ +2 V reversible electrostatic gating window is then shown to enable wide-range modulation of electron density and transport in EDLTs based on ultrathin (3.2 nm) CdO. Ten-fold variation in electron density is achieved, inducing a striking metal–insulator transition, 15-fold modulation of electron mobility, and a number of additional findings. These results advance the understanding of electrolyte gating mechanisms, improve the knowledge of transport in CdO, and open the door to voltage-tunable CdO-based devices, particularly in mid-infrared photonics and plasmonics.

EXPERIMENTAL DETAILS

Nominally-undoped CdO(001) films were deposited with thicknesses from 3 to 17 nm (the thickness being determined by grazing-incidence x-ray reflectivity), on 2 in.-diameter *r*-plane sapphire [$Al_2O_3(1\bar{1}02)$] wafers, by reactive high-power impulse magnetron sputtering (HiPIMS). Following prior work,[12,13,15,17–19,56] HiPIMS was done from a pure (99.9999%) Cd target, at 200–400 °C substrate temperature (lower temperatures were used for improved coalescence of the thinnest films), in 10 mTorr total pressure, with a 6:4 molar ratio of Ar/O_2. Films were then post-annealed for 30 min in 1 atm of O_2 at 635 °C to minimize V_O densities. Consistent with prior work,[12,13,15,17–19,56] substantial V_O concentrations remain, resulting in unintentionally *n*-doped films (as noted above, V_O are

understood to be shallow donors in CdO[8,11,21] and dangling bonds at the CdO surface also generate donor states[57]). This is illustrated in Fig. S1 in the supplementary material, which shows the resistivity, Hall mobility, and Hall electron density of 3.2- and 15-nm-thick films. The unintentional doping is quite heavy (1–2 × 10^{20} cm^{-3}, in fact, degenerate), the resulting 300 K mobilities and resistivities being 65–235 cm^2 V^{-1} s^{-1} and 0.38–0.24 mΩ cm (Fig. S1). Al_2O_3/CdO wafers were then diamond scribed into ∼5 × 10 mm^2 pieces for EDLT fabrication, as shown in Fig. 1(a). As in our prior work on other materials,[38,39,44,49,52,53] Ar-ion milling was employed in conjunction with a steel mask to pattern 2.5 × 2.5 mm^2 CdO channels, followed by deposition of Ti(or Mg)(20 nm)/Au(60 nm) four-wire contact and side-gate electrodes by room-temperature sputtering through a second mask [Fig. 1(a)]. EDLTs were then completed by laminating ∼50 μm-thick "cut-and-stick" solid-state ion gels on the devices, covering the channel, and connecting to the side-gate electrodes [Fig. 1(a)]. The ion gels were composed of 4:1-mass-ratio ionic liquid [1-ethyl-3-methylimidazolium bis(triflouromethylsulfonyl)amide (EMI-TFSI)] to polymer [poly(vinylidene fluoride-co-hexafluoropropylene) (PVDF-HFP)], prepared via spin coating on sacrificial substrates.

A first set of transport experiments, to establish gating mechanisms, employed EDLTs based on relatively thick (∼17 nm) CdO, at 300 K, in vacuum (<10^{-5} Torr), by either sweeping (at 5 mV/s) or stepping the gate voltage, V_g. For stepped-voltage experiments, V_g was applied for 20 min, followed by returning V_g to zero for 20 min, then repeating at successively larger or smaller V_g. DC measurements were made of the four-wire channel resistance, R (with a 50 mV source–drain voltage), and the gate current, I_g. Both before and after gating, structural characterization was performed via HRXRD on a Rigaku SmartLab XE (using Cu Kα radiation) and via contact-mode AFM in a Bruker Nanoscope V Multimode 8. For these characterizations, the overlying ion gels were removed with acetone. A second set of temperature (T)-dependent gating experiments was performed on EDLTs based on 3.2 nm-thick CdO films, in a Quantum Design Physical Property Measurement System, from 2 to 300 K in magnetic fields to 90 kOe. For these measurements, V_g was applied for 30 min at 275 K, the sample was cooled to low T, and the resistance and Hall effect data were taken on warming. V_g was applied (and I_g measured) using a Keithley 2400 source-measure unit, and four-wire van der Pauw sheet resistance (R_s) measurements (DC) were made using a Keithley 2400 source-measure unit or a Keithley 220 current source with a Keithley 2002 voltmeter. Excitation levels were selected to avoid self-heating and/or non-Ohmicity.

RESULTS AND DISCUSSION

As already noted, Fig. 1(a) shows a schematic of our CdO-based EDLTs. The first experiments with these focused on determining the active gating mechanisms. Following an approach established in our prior work, including on several oxides,[33,38,52,53] Figs. 1(b)–1(e) show the results of stepped-V_g measurements. In this approach, progressively decreasing [Fig. 1(b)] and increasing [Fig. 1(d)] stepped gate voltages are applied, on a 20-min-on/20-min-off cycle. The response of the CdO channel resistance is then tracked through the time (t) dependence of R/R_0, where R is the channel resistance and R_0 is its t = 0 (initial) value. As shown in Figs. 1(b) and 1(c), the response at negative V_g is near ideal. Specifically, progressively larger negative V_g induces progressively larger R/R_0, consistent with simple electrostatic depletion of these initially n-type CdO films. As an aside, we note that while the V_g response here is on minute time scales, this is due to the side-gate architecture [Fig. 1(a)], rather than an intrinsic limitation of EDLTs.[32,33] This device design enables rapid, high-throughput fabrication and exploration of new materials, particularly with cut-and-stick ion gels (as well as *operando* characterization[45,49,51,53–55]), but puts macroscopic distances between the channel and side gate electrodes, slowing the operation.[32,33] More importantly, Fig. 1(c) shows that R/R_0 returns to close to 1.0 after each V_g removal (within 20% in the worst case), strongly supporting a volatile, reversible gating mechanism, consistent with simple EDL charging.[31–33,35,37,38,40] This is reinforced by Fig. 1(f), which shows the V_g dependence of R_{on}/R_0 and R_{off}/R_0, where R_{on} and R_{off} are the magnitudes of R after the full 20 min durations of the "on" and "off" V_g cycles. These ratios thus probe the "gate effect" and "nonvolatility," respectively.[33,38,52,53] As can be seen in Fig. 1(f), negative gate biases result in increasingly large R_{on}/R_0, i.e., increasing gate effects, but with negligible R_{off}/R_0, i.e., little nonvolatility (R_{off}/R_0 is within 20% of unity). The negative V_g results in Figs. 1(b), 1(c), and 1(f) thus evidence an essentially entirely non-volatile, reversible gate effect, consistent with an electrostatic mechanism.

Continuing to positive V_g, Figs. 1(d)–1(f) show that the above trends initially continue, at least up to ∼1 V. Specifically, R/R_0 falls beneath 1, with small R_{off}/R_0, consistent with reversible, volatile, electron accumulation. An abrupt and dramatic change in behavior occurs at ∼2 V and above, however, where R_{on}/R_0 and R_{off}/R_0 both rapidly increase to positive values, i.e., large gate-induced resistance changes that are essentially entirely nonvolatile. The $I_g(V_g)$ data in Fig. 1(g) (from a 5 mV s^{-1} sweep) provide the first hint to the origin of this behavior. This trace reveals the usual crossover from low magnitudes of I_g to larger, hysteretic I_g at the largest magnitudes of both positive and negative V_g (due to the approach to the edges of the ion gel electrochemical stability window),[32,43] but with a clear additional feature around +2.5 V. Such I_g peaks typically indicate electrochemical activity in the gated film,[38,45,58] and we thus performed post-gating HRXRD and AFM characterization to probe for irreversible changes in structure, chemistry, or morphology after positive V_g application.

Figure 2(a) first shows specular wide-angle HRXRD, in an angular range that captures both the Al_2O_3 $1\bar{1}02$ and CdO 002 reflections, before applying an ion gel ("no gel") and after applying a gel then gating to 0, 1, 2, and 3 V. These data were again taken on 2.5 × 2.5 mm^2, 17 nm-thick films. The "no gel" case reveals only 00l reflections (confirmed on wider scans), with the Laue fringes indicating relatively low roughness [AFM measurements discussed below confirm a clear "step and terrace" morphology with root-mean-square (RMS) roughness as low as ∼1 nm]. The notable features with increasing V_g are the slight downshift in the CdO 002 peak position, the gradual dampening of Laue fringes, and the obvious peak broadening, with the +3 V peak additionally exhibiting clear asymmetry. Some of these features are illustrated more clearly in Figs. 2(b) and 2(c), which show the V_g dependence of the resulting c-axis lattice parameter and Scherrer length (Λ). The former is extracted from the peak position, the latter from the width, via the Scherrer formula. From Fig. 2(b), increasing positive gate voltages are found

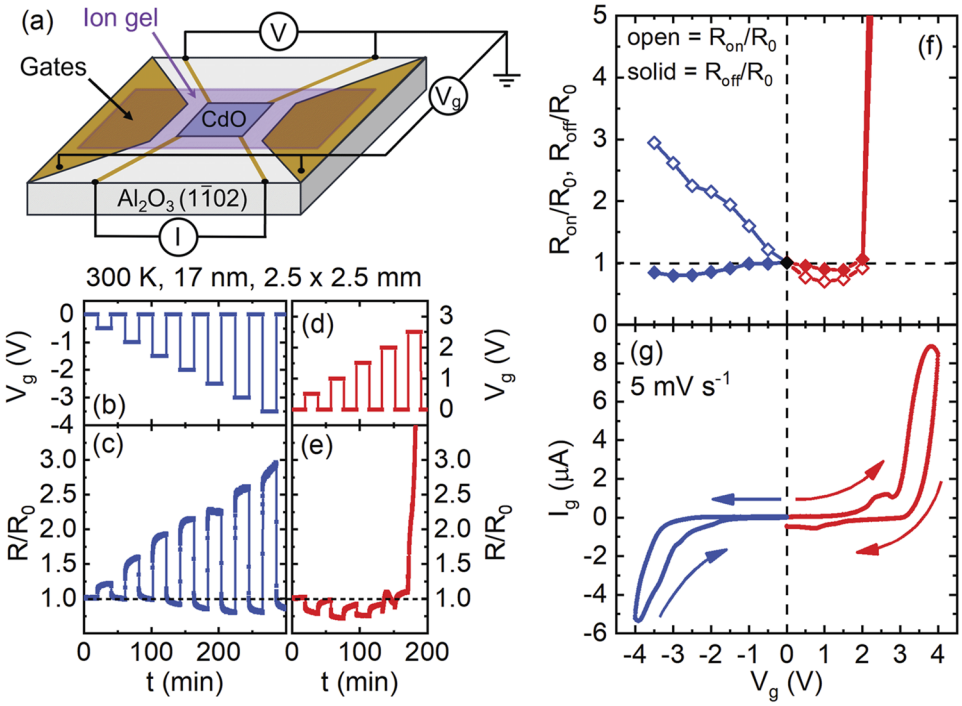

FIG. 1. (a) Schematic EDLT showing the Al_2O_3 substrate (gray), CdO channel (blue), ion gel (purple), gate electrodes (yellow), and four-wire measurement electrodes (yellow). *I* and *V* are the measurement current and voltage, and V_g is the gate voltage. (b) and (c) V_g vs time (*t*) and R/R_0 vs *t* (where *R* is the channel resistance and R_0 is its $t = 0$ value) during the negative-V_g (blue) stepped measurements described in the text. (d) and (e) The same data as in (b) and (c) but for positive V_g (red). The horizontal dashed line in (c) and (e) is at $R/R_0 = 1$. (f) V_g dependence of the R/R_0 *during* V_g application (the gate effect, R_{on}/R_0) and the R/R_0 *after returning* V_g *to zero* (the nonvolatility, R_{off}/R_0). (g) Gate current (I_g) vs V_g during a 5 mV s^{-1} sweep. The $V_g < 0$ (blue) and $V_g > 0$ (red) curves were collected on separate, nominally identical, devices. All data are for 17 nm-thick CdO films from the same wafer and were acquired at 300 K.

to induce non-trivial increases in *c*, approaching the relaxed bulk value for CdO (horizontal red dashed line). As shown in Fig. S2 in the supplementary material, the 002 diffraction peak at +3 V can alternatively be fitted as a superposition of two peaks, resulting in the two lattice parameters shown as open diamonds in Fig. 2(b). One lies very close to the relaxed bulk position and the other corresponds to a substantially increased lattice parameter. Correspondingly, Fig. 2(c) reveals a gradual decrease in *c*-axis Scherrer length with increasing positive V_g. Small associated changes in the CdO 002 rocking curve also occur [Fig. 1(a), inset]. These rocking curves are composed of narrow (~0.07°-wide) and broad (~1.2°-wide) components (typically associated with defect-poor and defect-rich regions), with the broad component decreasing slightly in relative intensity with V_g.

The contact-mode AFM scans shown in Figs. 2(d)–2(g) provide critical additional insight. Figure 2(d) first establishes low roughness (RMS values are shown in each panel) and a "terrace and step" morphology in as-grown films. Quantitative analysis suggests >1 nm-high steps, consistent with the typically observed surface morphology of *r*-Al_2O_3 substrates. Equivalent AFM scans after gating at −3 V [Fig. 2(e)] and +2.5 V [Fig. 2(f)] indicate that this "terrace and step" morphology is essentially preserved, but with clear additional ~50 nm-sized surface features. The latter have been previously observed after ion gel gating of oxide films and are simply due to the residual ion gel not fully removed after gating, as confirmed by x-ray photoelectron spectroscopy detection of, *e.g.*, fluorine.[52] The increased RMS roughnesses of ~3 to 4 nm derive from these features. Aside from this incomplete ion gel removal, the images in Figs. 2(e) and 2(f) evidence no major change in the surface morphology of the CdO itself. This situation changes conspicuously after gating to +3 V, however, Fig. 2(g) revealing major alterations in surface morphology, including the emergence of clear pitting. The pits range in depth from 10 to 15 nm, approaching the as-grown film thickness, and the RMS surface roughness thus increases dramatically, to >6 nm.

Piecing together the positive-V_g results from HRXRD and AFM, we conclude a gradual relaxation toward the bulk lattice parameter [Fig. 2(a)], that some portion of the film has substantially increased lattice parameter at the highest V_g [Figs. 2(a) and S2], progressively decreased out-of-plane Scherrer length [Fig. 2(c)], and the abrupt onset of surface pitting at the highest V_g [Fig. 2(g)]. We believe that these results can be simply and consistently interpreted in terms of *etching* of the CdO film at sufficiently large positive V_g, ultimately leading to etch pits and abrupt surface degradation. Sufficiently large positive gate voltages are known to lead to etching and eventual formation of etch pits in electrolyte-gated materials, two examples being $La_{1-x}Sr_xCoO_{3-\delta}$[52] and FeSe.[59] In $La_{1-x}Sr_xCoO_{3-\delta}$; for example, etch pits can form at large positive V_g, at an areal density consistent with threading dislocation densities at the substrate surface,[52] suggesting that the pits form at dislocation cores, as in acid etching of bulk oxides.[60] Notably, the acid etch rate of CdO is notoriously high, with rapid etching occurring even in dilute acid.[61] Obviously important in this context is that positive-V_g gating in EDLTs of this type is widely thought to induce electrolysis of residual H_2O in ionic liquids and gels,[32,33,45,51] thereby generating H^+. We propose that such an environment at the electrolyte/oxide interface essentially induces acidic conditions at the CdO film surface, leading to etching {thus decreasing the film thickness and, therefore, the Scherrer length [see Fig. 2(c)]}, eventual etch pit formation [Fig. 2(g)], the onset of strain relaxation [Fig. 2(b)],

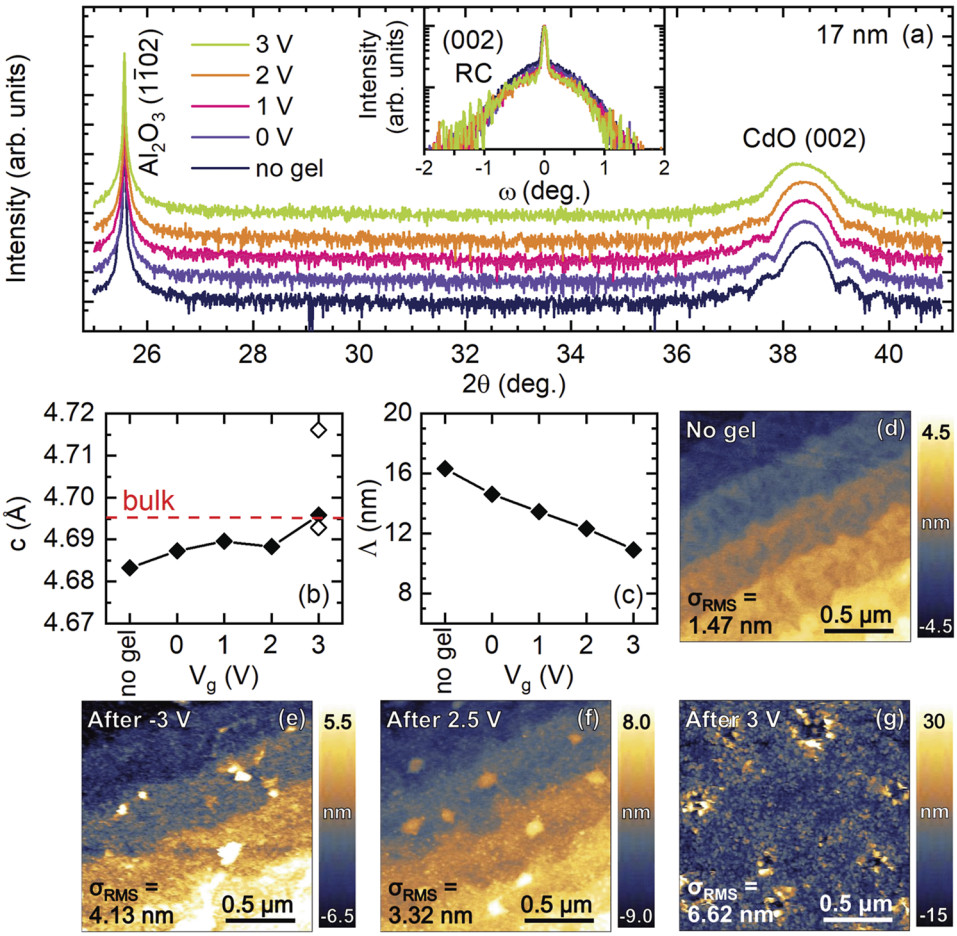

FIG. 2. (a) Specular high-resolution x-ray diffraction scans ($\log_{10}$-scale intensity vs 2θ) on a 2.5 × 2.5 mm^2 CdO film before ("no gel") and after ion-gel gating at various gate voltages (V_g), with the curves vertically offset for clarity. Substrate and film reflections are labeled. Inset: Corresponding rocking curves (RCs) ($\log_{10}$-scale, normalized) through the CdO 002 peak for each V_g in (a). (b) Out-of-plane lattice parameter (c) vs V_g. The horizontal red dashed line corresponds to bulk CdO, and the open diamonds at 3 V are the results of a multi-peak fit to the 3 V curve in (a) (see Fig. S2 in the supplementary material for more details). (c) Out-of-plane Scherrer length vs V_g. In (b) and (c), values before gating are labeled "no gel." (d)–(g) Contact-mode atomic force microscopy images (2 × 2 μm^2) before gating (d), after −3 V (e), after +2.5 V (f), and after +3 V (g). Surface height color scales are shown to the right of each image, and the extracted surface roughness (σ_{RMS}) is shown in each image. All data are for 17 nm-thick CdO films from the same wafer.

and likely highly O-deficient regions (or possibly H-doped[21,24,25] regions) with expanded lattice parameters [Figs. 2(b) and S2]. Some contribution to the decrease in Scherrer length in Fig. 2(c) could thus also arise from microstrain (i.e., lattice parameter inhomogeneity) effects. These various sources of film degradation in fact lead to channel resistance increases [Figs. 1(e) and 1(f)], limiting the useful bias window in these CdO EDLTs to $-4\ \text{V} < V_g < +2\ \text{V}$.

The origin of the simple electrostatic gating mechanism in the $-4\ \text{V} < V_g < +2\ \text{V}$ window is also of interest. We propose that this is yet further evidence for the recent claim that, in inorganic materials, predominantly electrostatic electrolyte gating mechanisms tend to arise in cases where the ambient-temperature diffusivities (D) of the lowest formation energy point defects are negligible.[33] In CdO, on the basis of results in this paper (*e.g.*, Fig. S1) and prior work,[8,11,21] V_O are likely the most relevant defects in this context. Based both on the close-packed rock-salt CdO structure (which would be expected to generate large energy barriers for oxygen migration) and prior data,[62] low diffusivity of V_O is expected in CdO films. Based on the data of Haul and Just, for example, on bulk CdO crystals,[62] extrapolation down to 500 °C already yields $D_{Vo} \sim 10^{-20}$ cm^2 s^{-1}, a very low diffusion coefficient (smaller, in fact, than in $BaSnO_3$, an exemplar for electrostatic response to electrolyte gating[38]); extrapolation to room temperature would yield yet smaller D_{Vo}. Within the recently published framework,[33] this will lead to a truly negligible diffusion length for V_O ($l_{Vo} = (D_{Vo}t)^{1/2} \ll 1$ Å) under our gating conditions (300 K, minute time scales), making it essentially impossible to proliferate any gate-induced interfacial V_O to non-negligible depths, regardless of the V_O formation energy. This favors electrostatic over electrochemical gating mechanisms,[33] exactly as we observe in the $-4\ \text{V} < V_g < +2\ \text{V}$ window. CdO is thus a rather unique case in this context, where such an electrostatic gate response is abruptly cut off at relatively low positive V_g by high acid etchability.[61] As a final comment on gating mechanisms, we note that H is also understood to be a shallow donor in CdO[21,24,25] and can be incorporated by annealing in H_2 at ~300 °C.[24,25] We thus cannot rule out that this also plays some role in the electrolyte gating of CdO in the $-4\ \text{V} < V_g < +2\ \text{V}$ window, although the time scales associated with the volatility and reversibility in Figs. 1(a)–1(e) would require extraordinary H ingress/egress rates, likely inconsistent with the elevated temperatures required to thermally dope H into CdO films.[24,25]

With an appreciation and understanding of the CdO electrolyte gating mechanisms in hand, Fig. 3 focuses solely on the $-4\ \text{V} < V_g < +2\ \text{V}$ reversible window, switching to ultrathin (3.2 nm)

CdO films. The low thickness is employed here to ensure a volumetric electrostatic gate effect, through the majority of the film thickness, thereby maximizing gate-induced changes in transport and eliminating current shunting via underlying ungated (V_O-doped) regions. This requires thicknesses of the order of the Thomas–Fermi electrostatic screening length, which we estimate, at the initial three-dimensional (3D) free electron densities of ~10^{20} cm^{-3} in Fig. S1, to be ~2 nm. Significantly, and as mentioned below, this reduction in film thickness from 17 to 3.2 nm increases the doping level slightly and decreases the room-temperature and low-temperature mobilities from 235 and 343 cm^2 V^{-1} s^{-1} to 65 and 80 cm^2 V^{-1} s^{-1}, respectively (Fig. S1). Figure 3(a) first shows V_g-dependent measurements of the T dependence of the CdO sheet resistance, R_s (left axis), or alternatively the resistivity, ρ (right axis). The latter is estimated using the full 3.2 nm film thickness. The ungated CdO film ["no gel," the dashed line in Fig. 3(a)] exhibits $R_s \approx 10^3$ Ω, with notably weak T dependence, unambiguously indicating the metallic character. This is confirmed in Fig. S3(a), which reveals clearly finite conductivity as $T \to 0$ before gating. Applying an ion gel but maintaining $V_g = 0$ [the gray curve in Fig. 3(a)] results in minor changes in $R_s(T)$, likely due to a chemical-affinity-driven imbalance of ion-gel cations and anions at the interface with CdO. A positive gate voltage of 1 V (pink curve) then induces a decrease in $R_s(T)$, consistent with accumulation of additional electrons in the CdO. This positive-voltage R_s decrease is limited to only ~twofold, however, due to the quite heavy initial (V_O) doping and the fact that +2 V [the red curve in Fig. 3(a)] already induces slight degradation.

Consistent with the thickness being of the order of the screening length, negative V_g applications [blue curves in Fig. 3(a)] lead to a rapid increase in R_s and progressively more insulating $R_s(T)$. $V_g \leq -2$ V, in fact, induces $R_s > h/e^2 \approx 26$ kΩ [Fig. 3(a)], negative dR_s/dT [Fig. 3(a)], and near-zero $T \to 0$ extrapolation of the conductivity [Fig. S3(a)]. These observations clearly illustrate a V_g-driven metal–insulator transition due to electrostatic depletion, with the −3 V curve in Fig. 3(a) indicating unambiguous insulating behavior, which is rarely, if ever, reported in CdO. The behavior at this stage is Arrhenius like [see Fig. S3(b)], with an activation energy in the 0.4–0.5 eV range, which is, again, notably large for CdO,[11–14,17,18,22,26,27] certainly evidencing insulating character at −3 V. As shown in Fig. S4, at 225 K, the lowest T to which all V_g curves in Fig. 3(a) could be measured, the V_g-driven modulation of R_s across this metal–insulator transition in CdO thus reaches almost five orders of magnitude. As a final comment on Fig. 3(a), we note that the rather chaotic behavior of $R_s(T)$ at higher temperatures is well-known in EDLTs,[34,38,39,50] deriving from phenomena associated with the melting point/glass transition temperature of the ionic liquids/gels.

The EDLTs used for Fig. 3(a) were also used for V_g-dependent measurements of the Hall effect, at illustrative temperatures of 20 and 150 K. The Hall voltage was found to be simply linear in the magnetic field (to ±90 kOe) at all V_g and T at which the Hall effect could be measured, the safe assumption of a single dominant carrier type leading to the electron densities and mobilities shown in Figs. 3(b) and 3(c). For convenience, and by analogy to Figs. 3(a), Fig. 3(b) shows both the 2D Hall electron density (n_{2D}, left axis) and 3D Hall electron density (n, right axis), the latter calculated using the full film thickness (3.2 nm). The reversible electrostatic gating window is found to enable modulation of n_{2D} between 2 × 10^{13} and 2 × 10^{14} cm^{-2}, i.e., over an order of magnitude. This $O(10^{14}$ cm$^{-2})$ extent of 2D charge carrier density modulation is typical of oxide-semiconductor-based EDLTs.[34–36,38–40] More quantitatively, Fig. S5 shows the data of Fig. 3(b) on a linear scale, along with fits to $n_{2D} = n_0 + \left(\frac{C}{A}\right)V_g$, where n_0 is the initial 2D Hall electron density and (C/A) is the specific capacitance. This yields (C/A) = 4–9 μF cm^{-2}, increasing with increasing V_g (Fig. S5), likely reflecting the increasing density-of-states at the Fermi level across the insulator–metal transition.[31,36,63] The highest values, near 10 μF cm^{-2}, are typical of the effective

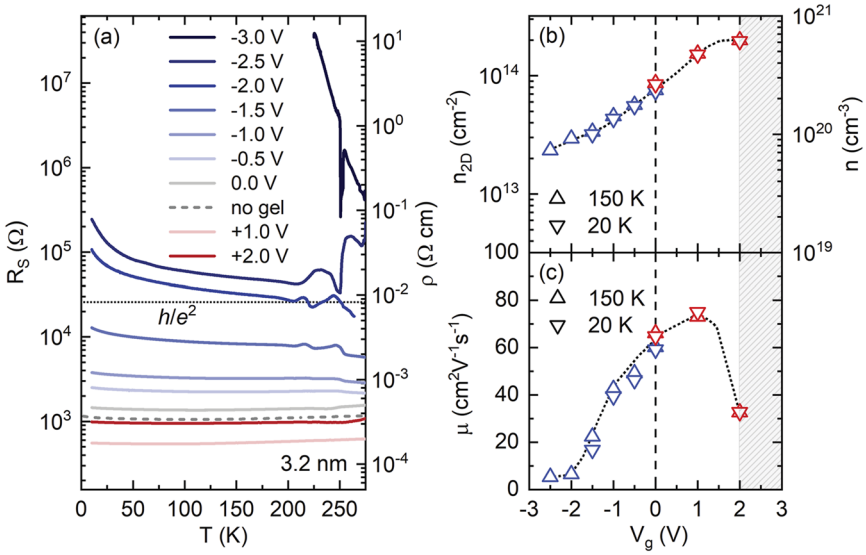

FIG. 3. (a) Temperature (T) dependence of the sheet resistance (R_s, left axis) and resistivity (ρ, right axis) of an ion-gel-gated 3.2 nm-thick CdO film before gating ("no gel") and after application of gate voltages (V_g) in the range −3.0 V < V_g < +2.0 V. The horizontal black dashed line marks h/e^2 = 26 kΩ. (b) and (c) V_g dependence of the Hall electron density (b) and Hall mobility (c) at 150 K (up triangles) and 20 K (down triangles). Both 2D (left axis) and 3D (right axis) Hall electron densities are shown in (b). As in Figs. 1(b)–1(g) and Fig. 3(a), red is used for positive V_g and blue is used for negative V_g. The dashed lines in (b) and (c) are guides to the eye, and the shaded region above 2 V marks the onset of degradation. All data are for 3.2 nm-thick CdO.

capacitances in semiconductor-based EDLTs,[31,32,34–36,38,64] yet further supporting a simple EDL charging mechanism. We additionally note that the Hall electron densities in Fig. 3(b) are essentially T-independent (i.e., the 20 and 150 K points overlap) in the $-1.5\ \text{V} \le V_g < +2\ \text{V}$ interval, indicating degenerate transport in that range, consistent with the metallic or close-to-metallic nature of the transport in this V_g range in Fig. 3(a). At smaller (i.e., more negative) V_g, 20 K values of the Hall electron density are not plotted in Fig. 3(b) as they could not be acquired due to carrier freeze-out/non-degenerate transport, consistent with $R_s(T)$ rising above $h/e^2 \approx 26\ \text{k}\Omega$ in Fig. 3(a). At −3 V, Hall effect data could not be recorded even at 150 K, consistent with the highly-insulating $R_s(T)$ in Fig. 3(a) [and Fig. S3(b)].

The corresponding Hall mobility (μ) in Fig. 3(c) is also informative. Unsurprisingly, as +2 V is approached, μ plummets, responding to the onset of etching-induced film degradation; this actually precedes slightly the detection of degradation via HRXRD and AFM, highlighting the sensitivity of the ultrathin-film mobility to this factor, which is duly reflected in R_s [Figs. 3(a) and S4]. Aside from this effect, μ monotonically decreases as V_g is decreased toward more negative values, i.e., with electron depletion [Fig. 3(c)]. This corresponds to increasing μ with increasing n, as frequently encountered in oxide semiconductors, and often ascribed to improved screening of charged defects with increased carrier density.[4–6,38–41] This is commonly followed by a regime where μ decreases at the highest n, for example, due to ionized dopant scattering, resulting in a mobility peak.[4–6,38–41] Prior work on CdO films as a function of conventional chemical doping revealed exactly this, $\mu(n)$ peaking in the 10^{19}–$10^{20}\ \text{cm}^{-3}$ range.[11–13,17,18,26] The fact that the electrolyte-gated mobility in Fig. 3(c) continues to rise up to $V_g = +1$ V, where the induced electron density reaches $n \approx 5 \times 10^{20}\ \text{cm}^{-3}$, limited only by the onset of film degradation at positive V_g, is thus of interest. This could be related to ion-gel-induced electron scattering (across the electrolyte/oxide interface)[39,65,66] being weaker than the ionized impurity scattering in conventionally-doped films. Moreover, noteworthy in Fig. 3(c) is the T dependence of μ. This inverts from the 20 K data points being below the 150 K data points at low μ to the 20 K data points being at or above the 150 K data points at high μ, reflecting the expected crossover to phonon-limited mobility. This crossover to phonon-limited $\mu(T)$ with increasing V_g (and thus, Hall density) in Fig. 3(c) is akin to the crossover to phonon-limited mobility with increasing film thickness in Fig. S1(b).

Notably, the overall mobility modulation in Fig. 3(c) is from 5.3 to $75\ \text{cm}^2\ \text{V}^{-1}\ \text{s}^{-1}$, i.e., a factor of 15. In totality, these ultrathin CdO EDLTs thus achieve modulation of the 2D electron density, mobility, and sheet resistance of factors of ~10, ~15, and almost 10^5, respectively (Figs. 3 and S4). While these values are already encouraging, and are particularly interesting in terms of potential voltage-tunability of photonic and plasmonic devices,[11–14,17,18] it should be stressed that further improvements are possible. Specifically, the only factors limiting the extents of these modulations are the quite heavy unintentional doping of the CdO films [Figs. S1, 3(a), and 3(b)] and the reduced electron mobility in the ultrathin limit [Figs. S1 and 3(c)]. Improvements in these factors via further refinement of deposition conditions, post-deposition treatment, substrate/buffer layer usage, or carefully designed capping layers (to mitigate surface accumulation effects[25,57] and/or surface scattering), would pave the way to yet stronger modulations of n_{2D}, n, R_s, ρ, etc., of high interest for applications.

SUMMARY

Ion-gel-based electrolyte gating of epitaxial CdO(001) films has been investigated. Initial relatively-thick-film results from transport, x-ray diffraction, and atomic force microscopy provided clear evidence for a wide window of reversible electrostatic gating, from −4 to +2 V, ascribed to low ambient-temperature oxygen vacancy diffusivity in the rock-salt structure of CdO. At higher gate voltages, abrupt film degradation was observed, eventually resulting in film etching. This was ascribed to the low acid etch resistance of CdO, with large positive gate voltages leading to the accumulation of substantial concentrations of H^+ at the film surface, from electrolysis of residual H_2O in the ion gels. With these results in hand, reversible electrostatic gating of ultrathin (3.2 nm-thick) CdO films in the −4 to +2 V window was shown to induce a striking metal–insulator transition, ten-fold modulation of the free electron density (from depletion to $2 \times 10^{13}\ \text{cm}^{-2}$ to accumulation to $2 \times 10^{14}\ \text{cm}^{-2}$), and associated 15-fold variation in electron mobility. These results further advance the growing mechanistic understanding of electrolyte gating mechanisms, shed new light on transport mechanisms in CdO, and pave the way to future low-power voltage-based modulation of carrier density for CdO-based tunable photonic and plasmonic devices.

SUPPLEMENTARY MATERIAL

See the supplementary material for additional transport data on ungated CdO films, x-ray diffraction peak shape analysis after gating, further analysis of gated transport data, and additional analysis of gate-voltage-dependent sheet resistance and Hall electron density.

ACKNOWLEDGMENTS

Work at the University of Minnesota (UMN) was primarily supported by the National Science Foundation (NSF) through the UMN MRSEC under Grant No. DMR-2011401. Parts of this work were carried out at the Characterization Facility, UMN, which receives partial support from the NSF through the MRSEC program. Portions of this work were also conducted in the Minnesota Nano Center, which is supported by the NSF through the National Nanotechnology Coordinated Infrastructure under Grant No. ECCS-2025124. Work at Pennsylvania State University was supported by the Office of Naval Research Grant No. N00014-22-12035, Army Research Office Research Grant No. W911NF-16-1-0406, and the Department of Defense (DoD) through the National Defense Science and Engineering Graduate (NDSEG) Fellowship Program.

AUTHOR DECLARATIONS

Conflict of Interest

The authors have no conflicts to disclose.

Author Contributions

H.W. and W.M.P. contributed equally to this work.

C.L. and J.-P.M. conceived of this study. E.L.R., A.C., and J.N. deposited the CdO films, under the supervision of J.-P.M. H.W., W.M.P., and V.C. performed the ion-gel gating experiments and related XRD and AFM, as well as associated analysis. C.L. and W.M.P. wrote the paper, with input from all authors.

Helin Wang: Data curation (equal); Formal analysis (equal); Investigation (lead); Methodology (lead); Visualization (supporting); Writing – review & editing (supporting). **William M. Postiglione**: Data curation (equal); Formal analysis (equal); Investigation (lead); Methodology (lead); Visualization (lead); Writing – original draft (supporting); Writing – review & editing (supporting). **Vipul Chaturvedi**: Formal analysis (supporting); Investigation (supporting); Methodology (supporting); Visualization (supporting); Writing – review & editing (supporting). **Evan L. Runnerstrom**: Investigation (supporting); Methodology (supporting); Writing – review & editing (supporting). **Angela Cleri**: Investigation (supporting); Methodology (supporting); Writing – review & editing (supporting). **Josh Nordlander**: Investigation (supporting); Methodology (supporting); Writing – review & editing (supporting). **Jon-Paul Maria**: Conceptualization (supporting); Funding acquisition (equal); Project administration (equal); Supervision (equal); Writing – review & editing (supporting). **Chris Leighton**: Conceptualization (lead); Formal analysis (supporting); Funding acquisition (lead); Investigation (supporting); Methodology (supporting); Project administration (lead); Supervision (lead); Visualization (supporting); Writing – original draft (lead); Writing – review & editing (lead).

DATA AVAILABILITY

The data that support the findings of this study are available within the article and its supplementary material or from the corresponding author upon reasonable request.

REFERENCES

[1] E. Fortunato, P. Barquinha, and R. Martins, Adv. Mater. **24**, 2945 (2012).
[2] M. Morales-Masis, S. De Wolf, R. Woods-Robinson, J. W. Ager, and C. Ballif, Adv. Electron. Mater. **3**, 1600529 (2017).
[3] H. Khamh, E. Sachet, K. Kelly, J.-P. Maria, and S. Franzen, J. Mater. Chem. C **6**, 8326 (2018).
[4] A. Prakash and B. Jalan, Adv. Mater. Interfaces **6**, 1900479 (2019).
[5] W. Nunn, T. K. Truttmann, and B. Jalan, J. Mater. Res. **36**, 4846 (2021).
[6] J. Shi, J. Zhang, L. Yang, M. Qu, D. C. Qi, and K. H. L. Zhang, Adv. Mater. **33**, 2006230 (2021).
[7] T. K. Lakshmanan, J. Electrochem. Soc. **110**, 548 (1963).
[8] F. P. Koffyberg, Phys. Lett. A **30**, 37 (1969).
[9] K. Tanaka, A. Kunioka, and Y. Sakai, Jpn. J. Appl. Phys. **8**, 681 (1969).
[10] J. S. Choi, Y. H. Kang, and K. H. Kim, J. Phys. Chem. **81**, 2208 (1977).
[11] E. Sachet, C. T. Shelton, J. S. Harris, B. E. Gaddy, D. L. Irving, S. Curtarolo, B. F. Donovan, P. E. Hopkins, P. A. Sharma, A. L. Sharma, J. Ihlefeld, S. Franzen, and J.-P. Maria, Nat. Mater. **14**, 414 (2015).
[12] K. P. Kelley, E. Sachet, C. T. Shelton, and J.-P. Maria, APL Mater. **5**, 076105 (2017).
[13] E. L. Runnerstrom, K. P. Kelley, E. Sachet, C. T. Shelton, and J.-P. Maria, ACS Photonics **4**, 1885 (2017).
[14] Y. Yang, K. Kelley, E. Sachet, S. Campione, T. S. Luk, J.-P. Maria, M. B. Sinclair, and I. Brener, Nat. Photonics **11**, 390 (2017).
[15] E. L. Runnerstrom, K. P. Kelley, T. G. Folland, J. R. Nolen, N. Engheta, J. D. Caldwell, and J.-P. Maria, Nano Lett. **19**, 948 (2019).
[16] Y. Yang, J. Lu, A. Manjavacas, T. S. Luk, H. Liu, K. Kelley, J.-P. Maria, E. L. Runnerstrom, M. B. Sinclair, S. Ghimire, and I. Brener, Nat. Phys. **15**, 1022 (2019).
[17] K. P. Kelley, E. L. Runnerstrom, E. Sachet, C. T. Shelton, E. D. Grimley, A. Klump, J. M. LeBeau, Z. Sitar, J. Y. Suen, W. J. Padilla, and J.-P. Maria, ACS Photonics **6**, 1139 (2019).
[18] J. R. Nolen, E. L. Runnerstrom, K. P. Kelley, T. S. Luk, T. G. Folland, A. Cleri, J.-P. Maria, and J. D. Caldwell, Phys. Rev. Mater. **4**, 025202 (2020).
[19] A. Cleri, J. Tomko, K. Quiambao-Tomko, M. V. Imperatore, Y. Zhu, J. R. Nolen, J. Nordlander, J. D. Caldwell, Z. Mao, N. C. Giebink, K. P. Kelley, E. L. Runnerstrom, P. E. Hopkins, and J.-P. Maria, Phys. Rev. Mater. **5**, 035202 (2021).
[20] F. P. Koffyberg, Phys. Rev. B **13**, 4470 (1976).
[21] M. Burbano, D. O. Scanlon, and G. W. Watson, J. Am. Chem. Soc. **133**, 15065 (2011).
[22] A. Wang, J. R. Babcock, N. L. Edleman, A. W. Metz, M. A. Lane, R. Asahi, V. P. Dravid, C. R. Kannewurf, A. J. Freeman, and T. J. Marks, Proc. Natl. Acad. Sci. U. S. A. **98**, 7113 (2001).
[23] P. H. Jefferson, S. A. Hatfield, T. D. Veal, P. D. C. King, C. F. McConville, J. Zúñiga–Pérez, and V. Muñoz–Sanjosé, Appl. Phys. Lett. **92**, 022101 (2008).
[24] A. A. Dakhel, Semicond. Sci. Technol. **23**, 055017 (2008).
[25] P. D. C. King, T. D. Veal, P. H. Jefferson, J. Zúñiga-Pérez, V. Muñoz-Sanjosé, and C. F. McConville, Phys. Rev. B **79**, 035203 (2009).
[26] C. P. Liu, Y. Foo, M. Kamruzzaman, C. Y. Ho, J. A. Zapien, W. Zhu, Y. J. Li, W. Walukiewicz, and K. M. Yu, Phys. Rev. Appl. **6**, 064018 (2016).
[27] M. Yan, M. Lane, C. R. Kannewurf, and R. P. H. Chang, Appl. Phys. Lett. **78**, 2342 (2001).
[28] Y.-W. Huang, H. W. H. Lee, R. Sokhoyan, R. A. Pala, K. Thyagarajan, S. Han, D. P. Tsai, and H. A. Atwater, Nano Lett. **16**, 5319 (2016).
[29] Y. Lee, J. Yun, S. J. Kim, M. Seo, S.In, H. D. Jeong, S. Y. Lee, N. Park, T. D. Chung, and B. Lee, Adv. Opt. Mater. **8**, 2001256 (2020).
[30] G. K. Shirmanesh, R. Sokhoyan, P. C. Wu, and H. A. Atwater, ACS Nano **14**, 6912 (2020).
[31] S. Z. Bisri, S. Shimizu, M. Nakano, and Y. Iwasa, Adv. Mater. **29**, 1607054 (2017).
[32] C. Leighton, Nat. Mater. **18**, 13 (2019).
[33] C. Leighton, T. Birol, and J. Walter, APL Mater. **10**, 040901 (2022).
[34] H. Shimotani, H. Asanuma, A. Tsukazaki, A. Ohtomo, M. Kawasaki, and Y. Iwasa, Appl. Phys. Lett. **91**, 082106 (2007).
[35] H. Yuan, H. Shimotani, A. Tsukazaki, A. Ohtomo, M. Kawasaki, and Y. Iwasa, Adv. Funct. Mater. **19**, 1046 (2009).
[36] W. Xie, X. Zhang, C. Leighton, and C. D. Frisbie, Adv. Electron. Mater. **3**, 1600369 (2017).
[37] X. Leng, A. T. Bollinger, and I. Bozovic, Sci. Rep. **6**, 31239 (2019).
[38] H. Wang, J. Walter, K. Ganguly, B. Yu, G. Yu, Z. Zhang, H. Zhou, H. Fu, M. Greven, and C. Leighton, Phys. Rev. Mater. **3**, 075001 (2019).
[39] H. Wang, A. Prakash, K. Reich, K. Ganguly, B. Jalan, and C. Leighton, APL Mater. **8**, 071113 (2020).
[40] L. R. Thoutam, J. Yue, A. Prakash, T. Wang, K. E. Elangovan, and B. Jalan, ACS Appl. Mater. Interfaces **11**, 7666 (2019).
[41] A. K. Rajapitamahuni, A. K. Manjeshwar, A. Kumar, A. Datta, P. Ranga, L. R. Thoutam, S. Krishnamoorthy, U. Singisetti, and B. Jalan, ACS Nano **16**, 8812 (2022).
[42] K. H. Lee, M. S. Kang, S. Zhang, Y. Gu, T. P. Lodge, and C. D. Frisbie, Adv. Mater. **24**, 4457 (2012).
[43] S. H. Kim, K. Hong, W. Xie, K. H. Lee, S. Zhang, T. P. Lodge, and C. D. Frisbie, Adv. Mater. **25**, 1822 (2013).
[44] J. Walter, T. Charlton, H. Ambaye, M. R. Fitzsimmons, P. P. Orth, R. M. Fernandes, and C. Leighton, Phys. Rev. Mater. **2**, 111406(R) (2018).
[45] N. Lu, P. Zhang, Q. Zhang, R. Qiao, Q. He, H.-B. Li, Y. Wang, J. Guo, D. Zhang, Z. Duan, Z. Li, M. Wang, S. Yang, M. Yan, E. Arenholz, S. Zhou, W. Yang, L. Gu, C.-W. Nan, J. Wu, Y. Tokura, and P. Yu, Nature **546**, 124 (2017).

[46]H. Ji, J. Wei, and D. Natelson, Nano Lett. **12**, 2988 (2012).
[47]J. Jeong, N. Aetukuri, T. Graf, T. D. Schladt, M. G. Samant, and S. S. P. Parkin, Science **339**, 1402 (2013).
[48]Q. Lu and B. Yildiz, Nano Lett. **16**, 1186 (2016).
[49]J. Walter, G. Yu, B. Yu, A. Grutter, B. Kirby, J. Borchers, Z. Zhang, H. Zhou, T. Birol, M. Greven, and C. Leighton, Phys. Rev. Mater. **1**, 071403(R) (2017).
[50]B. Cui, P. Werner, T. Ma, X. Zhong, Z. Wang, J. M. Taylor, Y. Zhuang, and S. S. P. Parkin, Nat. Commun. **9**, 3055 (2018).
[51]S. Ning, Q. Zhang, C. Occhialini, R. Comin, X. Zhong, and C. A. Ross, ACS Nano **14**, 8949 (2020).
[52]J. Walter, H. Wang, B. Luo, C. D. Frisbie, and C. Leighton, ACS Nano **10**, 7799 (2016).
[53]V. Chaturvedi, W. M. Postiglione, R. D. Chakraborty, B. Yu, W. Tabiś, S. Hameed, N. Biniskos, A. Jacobson, Z. Zhang, H. Zhou, M. Greven, V. E. Ferry, and C. Leighton, ACS Appl. Mater. Interfaces **13**, 51205 (2021).
[54]A. M. Perez-Muñoz, P. Schio, R. Poloni, A. Fernandez-Martinez, A. Rivera-Calzada, J. C. Cezar, E. Salas-Colera, G. R. Castro, J. Kinney, C. Leon, J. Santamaria, J. Garcia-Barriocanal, and A. M. Goldman, Proc. Natl. Acad. Sci. U. S. A. **114**, 215 (2017).
[55]B. Yu, G. Yu, J. Walter, V. Chaturvedi, J. Gotchnik, S. Hameed, J. W. Freeland, C. Leighton, and M. Greven, Appl. Phys. Lett. **116**, 201905 (2020).
[56]E. Radue, E. L. Runnerstrom, K. P. Kelley, C. M. Rost, B. F. Donovan, E. D. Grimley, J. M. LeBeau, J.-P. Maria, and P. E. Hopkins, Phys. Rev. Mater. **3**, 032201(R) (2019).
[57]D. T. Speaks, M. A. Mayer, K. M. Yu, S. S. Mao, E. E. Haller, and W. Walukiewicz, J. Appl. Phys. **107**, 113706 (2010).
[58]M. Wang, X. Sui, Y. Wang, Y. H. Juan, Y. Lyu, H. Peng, T. Huang, S. Shen, C. Guo, J. Zhang, Z. Li, H. B. Li, N. Lu, A. T. N'Diaye, E. Arenholz, S. Zhou, Q. He, Y. H. Chu, W. Duan, and P. Yu, Adv. Mater. **31**, 1900458 (2019).
[59]J. Shiogai, Y. Ito, T. Mitsuhashi, T. Nojima, and A. Tsukazaki, Nat. Phys. **12**, 42 (2016).
[60]K. Szot, W. Speier, R. Carius, U. Zastrow, and W. Beyer, Phys. Rev. Lett. **88**, 075508 (2002).
[61]Z. A. Peng and X. Peng, J. Am. Chem. Soc. **123**, 183 (2001).
[62]R. Haul and D. Just, J. Appl. Phys. **33**, 487 (1962).
[63]J. Ye, M. F. Craciun, M. Koshino, S. Russo, S. Inoue, H. Yuan, H. Shimotani, A. F. Morpurgo, and Y. Iwasa, Proc. Natl. Acad. Sci. U. S. A. **108**, 13002 (2011).
[64]P. Gallagher, M. Lee, T. A. Petach, S. W. Stanwyck, J. R. Williams, K. Watanabe, T. Taniguchi, and D. Goldhaber-Gordon, Nat. Commun. **6**, 6437 (2015).
[65]J. Nelson, K. V. Reich, M. Sammon, B. I. Shklovskii, and A. M. Goldman, Phys. Rev. B **92**, 085424 (2015).
[66]T. A. Petach, K. V. Reich, X. Zhang, K. Watanabe, T. Taniguchi, B. I. Shklovskii, and D. Goldhaber-Gordon, ACS Nano **11**, 8395 (2017).